ACS Catalysis

Research Article

pubs.acs.org/acscatalysis

Platinum Nanoparticle During Electrochemical Hydrogen Evolution: Adsorbate Distribution, Active Reaction Species, and Size Effect

Teck L. Tan,*[,†] Lin-Lin Wang,[‡] Jia Zhang,[†] Duane D. Johnson,[‡,§] and Kewu Bai[†]

[†]Institute of High Performance Computing, Agency for Science, Technology and Research, Singapore 138632, Singapore
[‡]Ames Laboratory, U.S. Department of Energy, 311 TASF, Iowa State University, Ames, Iowa 50011-3020, United States
[§]Department of Materials Science and Engineering, Iowa State University, Ames, Iowa 50011, United States

Supporting Information

ABSTRACT: For small Pt nanoparticles (NPs), catalytic activity is, as observed, adversely affected by size in the 1−3 nm range. We elucidate, via first-principles-based thermodynamics, the operation H* distribution and cyclic voltammetry (CV) during the hydrogen evolution reaction (HER) across the electrochemical potential, including the underpotential region ($U \leq 0$) that is difficult to assess in experiment. We consider multiple adsorption sites on a 1 nm Pt NP model and show that the characteristic CV peaks from different H* species correspond well to experiment. We next quantify the activity contribution from each H* species to explain the adverse effect of size. From the resolved CV peaks at the standard hydrogen electrode potential ($U = 0$), we first deduce that the active species for the HER are the partially covered (100)-facet bridge sites and the (111)-facet hollow sites. Upon evaluation of the reaction barriers at operation H* distribution and microkinetic modeling of the exchange current, we find that the nearest-neighbor (100)-facet bridge site pairs have the lowest activation energy and contribute to ∼75% of the NP activity. Edge bridge sites (fully covered by H*) per se are not active; however, they react with neighboring (100)-facet H* to account for ∼18% of the activity, whereas (111)-facet hollow sites contribute little. Extrapolating the relative contributions to larger NPs in which the ratio of facet-to-edge sites increases, we show that the adverse size effect of Pt NP HER activity kicks in for sizes below 2 nm.

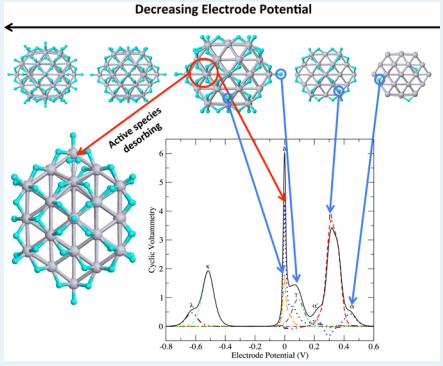

KEYWORDS: *first-principles, cluster expansion, adsorption isotherm, hydrogen evolution, hydrogen oxidation, cyclic voltammetry, catalysis, platinum, electrochemistry*

INTRODUCTION

The properties of nanoparticles (NPs) are highly dependent on their shape, size, composition, and structure. For catalyst design, control over these variables implies the ability to manipulate the quantity of different types of catalytic active sites on different facets, edges, and corners of the NP, which is key to optimizing the NP's activity and selectivity. Control over NP shape, size, and composition has been achieved for a number of transition metals and alloys[1−6] via solution-based synthesis. For Pt and its alloys,[1] the recent push for clean hydrogen fuels technologies[7,8] has led to a widespread electrochemical characterization of NPs of various shapes and sizes;[1,3,4,9−11] Pt is often the catalyst of choice for the key electrochemical reactions in these technologies, namely, the hydrogen oxidation/evolution reactions (HOR/HER)[12] and the oxygen reduction/evolution reactions (ORR/OER).[13]

From a catalyst design standpoint, first-principles computations have proved invaluable for understanding and predicting the electrocatalytic behavior of transition metal surfaces for the HER/HOR[12] and the ORR;[13] plotting their electrocatalytic activities against the calculated adsorption free energies of the reaction intermediates results in volcano curves in which the best catalysts, such as Pt, lie close to the top of the curve.[12,13] Nanoscaling further enhances catalyst performance, although this is not guaranteed for very small Pt NP for the HER/HOR and ORR, where the specific mass activity decreases with size.[14,15]

Thus far, theoretical explanations of adverse size effects on NP activity are indirectly deduced from (i) ideal surface models[16] or (ii) NP models with hypothetical adsorbate coverage.[17] A direct explanation has been elusive, partly because information on the adsorbate distribution on NP is scarce. To reliably determine the adsorbate distribution, adsorbate−adsorbate interactions have to be modeled, as is done for ideal surface catalysts, in which the thermodynamic behavior of adsorbates during catalytic operating conditions is simulated.[18−20] Such simulations allow for a direct visualization of the thermodynamically stable adsorbate distribution on the catalyst surfaces, giving valuable insights to possible active adsorption species and reaction intermediates. Compared with ideal surfaces, NPs pose a challenge because more symmetry-distinct adsorbate interactions have to be accounted for owing

Received: November 19, 2014
Revised: February 25, 2015
Published: March 2, 2015

DOI: 10.1021/cs501840c
ACS Catal. 2015, 5, 2376−2383

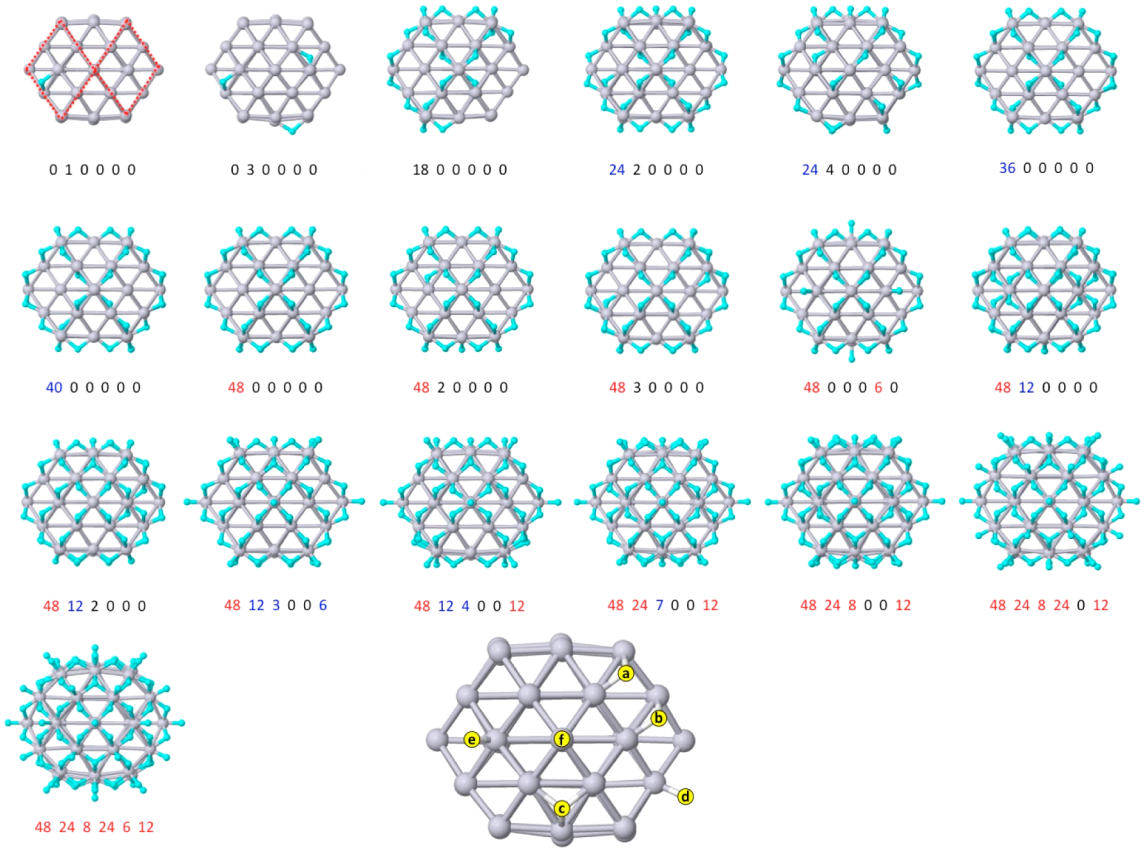

Figure 1. Groundstates of H* (cyan spheres) on Pt (gray spheres) NPs. Numbers below each groundstate correspond to the number of H* at each of the six symmetry-unique adsorption sites labeled on the NP at the bottom center, (a) b_e, (b) b_{100}, (c) h_{111}, (d) t_e, (e) t_{100}, and (f) t_c. Adsorption sites with 100% (>50%) H occupation have their numbers in red (blue). The groundstate with H* occupation {48, 12, 4, 0, 0, 12} is the lowest-energy configuration in our MC simulation at $U = 0$. The NP consists of six (100) facets (outlined in red for the first groundstate) and eight "triangular" (111) facets.

to the larger number of adsorption site types for NPs (different facets, edges, and corners).

The cluster expansion (CE) method[17,21−24] provides the most general tool to construct effective adsorbate−adsorbate interactions.[19,20,25−28] In addition to short-range pair interactions, the CE method includes both long-range and multibody effective interactions, which are essential for capturing the presence of minority adsorbate species that could be the key reaction inermediates.[19] We simulate hydrogen adsorption isotherms and the associated cyclic volatammetry (CV) using the CE method. We identify thermodynamically stable H* configurations on the NP catalyst during HER and the active species under realistic coverage, focusing on 1 nm size Pt NPs, using an ideal cuboctahedron, a commonly observable and synthesizable shape.[2,9,29]

To assess the NP activity during HER, we extract the thermodynamically stable H* configurations that are representative of the NP functioning under standard operating conditions of the hydrogen electrode. Using a representative H* configuration, we then evaluate H_2 desorption energy barriers and the exchange current via microkinetic modeling to quantify the activity contributions from each H* species. We show that the nearest neighbor bridge site pairs on the facets are the most active, contributing to ∼75% of the NP activity. Edge sites per se are not active; however, they react with neighboring H* on the (100) facet to account for ∼18% of the activity. The results explain previous deductions that facet sites are more catalytically active than edge sites[14,16] and affirm that the decrease in the ratio of facet-to-edge adsorption sites is the reason behind the observed adverse size effect of small NPs.

Another key result of this work is that our derived CV profile is comparable to those from experiments. To identify the different adsorption sites present on the NP surface, experiments compare the NP CV profiles[10,30] with those of model single-crystal surfaces[31−33] of Pt. The position and sharpness of the CV peaks are linked to surface orientation[31,32] and the presence of specific step edges and kinks.[34−38] By directly partitioning the CV profile into individual components to identify the H* species contributing to each of the peaks, our simulations offer an unambiguous association of the adsorbate species responsible for each CV peak. We found that the CV peaks agree with experimental ones. In addition, we identify a new peak (and its origin) close to the standard hydrogen electrode potential that can explain the observations in some experiments.[39,40]

METHODOLOGY

We used the Vienna ab initio simulation package (VASP)[41,42] within a projected augmented wave (PAW) basis[43] along with the revised PBE functional[44] to obtain the DFT adsorption energies and the climbing image nudged elastic band method[45] for energy barrier calculations (details given in the Supporting Information (SI)). To compare the relative stabilities of the H* configurations, σ, on the NPs, we define the adsorption energy as

DOI: 10.1021/cs501840c
ACS Catal. 2015, 5, 2376−2383

Table 1. Energy terms in eV at T = 298 K[a]

H type	ZPE	ΔE_{ZPE}	F_{vib}	$\Delta F'$ [d]	$\Delta E_{ZPE} + \Delta F'$	E_{ads}^{single}	$E_{ads}^{single} + \Delta E_{ZPE} + \Delta F'$
H* (b_e)	0.168	0.033	−0.005[b]	0.166	0.200	−0.473	−0.273
H* (b_{100})	0.174	0.039	−0.004[b]	0.167	0.207	−0.605	−0.398
H* (h_{111})	0.126	−0.009	−0.004[b]	0.167	0.158	−0.146	0.012
H* (t_e)	0.173	0.038	−0.016[b]	0.155	0.193	−0.442	−0.249
H* (t_{100})	0.186	0.051	−0.012[b]	0.159	0.210	−0.576	−0.366
H* (t_c)	0.171	0.036	−0.014[b]	0.157	0.194	−0.460	−0.266
H_2	0.271		−0.341[c]				

[a]The correction, $F_{vib} = E_{vib} - TS_{vib}$, is obtained from harmonic approximation.[19] E_{ads}^{single} is calculated via eq 1 on the basis of one adsorbed H*, i.e., $m = 1$. [b]Vibrational contributions only. [c]$F = E - TS = 0.062 - 0.403$. Values include vibrational, translational, and rotational contributions.[19,52] [d]$\Delta F'$ includes vibrational, translational, and rotational contributions; see eq 6.

$$E_{ads}(\sigma) = \left(E_{Pt-mH}(\sigma) - E_{Pt} - \frac{m}{2}E_{H_2}\right)/N \quad (1)$$

Here, E_{Pt} and $E_{H_2}$are the energies of the bare 55-atom Pt NP and the H_2 molecule. $E_{Pt-mH}(\sigma)$ is the (configuration-dependent) energy of the NP adsorbed with m H atoms, and $N = 122$ is the total number of adsorption sites. The fraction of adsorption sites occupied by H is given by $\theta = m/N$.

As shown in Figure 1, we consider six symmetry-distinct adsorption sites[17] for H on our model 55-atom Pt cuboctahedral NP. The bridge sites consist of 48 b_e and 24 b_{100} sites which are located at the NP edge and (100) facet, respectively. The atop sites consist of 24 t_e, 6 t_{100}, and 12 t_c sites, which are located on top of the center Pt atom at the edge, the center Pt atom on the (100) facet, and the corner Pt, respectively. For the (111) facet, we consider 8 h_{111} fcc-type hollow sites.

To model the effective interactions between neighboring H*, we construct a CE using the TTK[17,24,46−49] code we have developed. The optimally truncated CE reproduces well the DFT-calculated $E_{ads}(\sigma)$ and is used in Monte Carlo (MC) simulations to search for low-energy H* configurations and obtain the adsorption isotherms. Additional details are given in the Supporting Information.

RESULTS AND DISCUSSION

Low-Energy H* Configurations. For a single-H* adsorption, the b_{100} site is the most stable and $E_{ads}(b_{100}) < E_{ads}(t_{100}) < E_{ads}(b_e) < E_{ads}(t_c) < E_{ads}(t_e) < E_{ads}(h_{111})$. As shown in Table 1, their relative stabilities remain unchanged with zero-point energy (ZPE) and H* vibrational free energies (F_{vib}) corrections. Figure 1 shows the groundstate configurations obtained from the set of 452 DFT-calculated $E_{ads} + \Delta E_{ZPE}$ for H* configurations across $0 \le m \le 122$ (see Figure S2). These groundstates give an overview of where individual H atoms are adsorbed on the NP as coverage increases.

At very low θ, b_{100} sites are occupied first; however, the strong effective repulsion (see Table S1) between neighboring b_{100} sites, ∼0.19 eV (∼0.12 eV) for (next) nearest neighbors (n.n.), implies each (100) facet will have one occupied b_{100}, at most. Likewise, even though $E_{ads}(t_{100})$ is the second-lowest, the initial occupation of some b_{100} sites precludes occupation of t_{100} because the effective b_{100}−t_{100} repulsion is strong at ∼0.2 eV (see Table S1). In contrast, the relatively weak b_e−b_e and b_e−b_{100} repulsions (∼0.05 eV) allow the majority of H to occupy the b_e site for $N\theta \le 48$. When all b_e sites are occupied, the next H atoms will occupy one of the three remaining empty b_{100} sites, yielding a pair of occupied next-n.n. b_{100} on each (100) facet, obtaining $m = 60$. At this stage, adsorption on t_c, h_{111}, and the remaining n.n. b_{100} sites are energetically comparable, and they are filled up accordingly to reach $m = 92$. Thereafter, H occupies the t_e sites and, last, the t_{100} sites. The hcp hollow sites are not considered; their E_{ads} (−0.2 eV) is much higher compared with the bridge and atop sites. During DFT calculations, when low-energy b_e sites are occupied, the H*'s at the hcp site are unstable and get repelled into the neighboring vacant h_{111} site.

Electrochemical Reactions. The overall HER and its reverse, HOR, $H^+ + e^- \leftrightarrow (1/2)H_2$, could proceed via the Volmer−Heyrovsky or the Volmer−Tafel mechanisms.[12]

$$H^+ + e^- \rightarrow H^* \quad \text{(Volmer)} \quad (2)$$

$$H^* + H^* \rightarrow H_2(g) \quad \text{(Tafel)} \quad (3)$$

$$H^* + H^+ + e^- \rightarrow H_2(g) \quad \text{(Heyrovsky)} \quad (4)$$

For Pt catalysts, the Volmer's step is often assumed to be at quasi-equilibrium because its reaction barrier is much lower than that of the Tafel and Heyrovsky reactions.[50] Following the approach by Norskov et al.,[18] we define the free energy for the Volmer's reaction as

$$\Delta G = \Delta G_0 + eU \quad (5)$$

where U is the overpotential with respect to the standard hydrogen electrode. At $U = 0$, the reaction energy for the HER, $H^+ + e^- \rightarrow (1/2)H_2$, is defined to be zero at standard conditions ($T = 298$ K, $p = 1$ atm, pH = 0). As a result, ΔG_0 may be defined as the reaction free energy for $(1/2)H_2$ (g) → H* at standard conditions, which can be calculated as

$$\begin{aligned}\Delta G_0 &= \langle E_{ads}\rangle_\sigma + \Delta E_{ZPE} + \Delta F_{vib} + \Delta F_{tran} + \Delta F_{rot} \\ &= \langle E_{ads}\rangle_\sigma + \Delta E_{ZPE} + \Delta F' \end{aligned} \quad (6)$$

$$\Delta F_{vib} = \Delta E_{vib}(T) - T\Delta S_{vib} \quad (7)$$

Here, $\langle E_{ads}\rangle_\sigma$ is the configuration-averaged adsorption energy as defined in eq 1, which is obtained by MC simulation using the CE formalism. ΔE_{ZPE}, $\Delta E_{vib}(T)$, and ΔS_{vib} are the differences in ZPE, vibrational free energy and entropy between the adsorbed H states and the H_2 gas, respectively. ΔF_{tran} and ΔF_{rot} are differences in translational and rotational free energies, which arise solely from the H_2 gas. The values are approximated from a single adsorbed H* (see Table 1), and their derivation[19,51,52] is explained in the SI. Our MC simulations are performed under the condition $\Delta G = 0$ to obtain the H adsorption isotherms.

Coverage vs Electrochemical Potential. We plot in Figure 2 the simulated adsorption isotherm and CV curves

DOI: 10.1021/cs501840c
ACS Catal. 2015, 5, 2376−2383

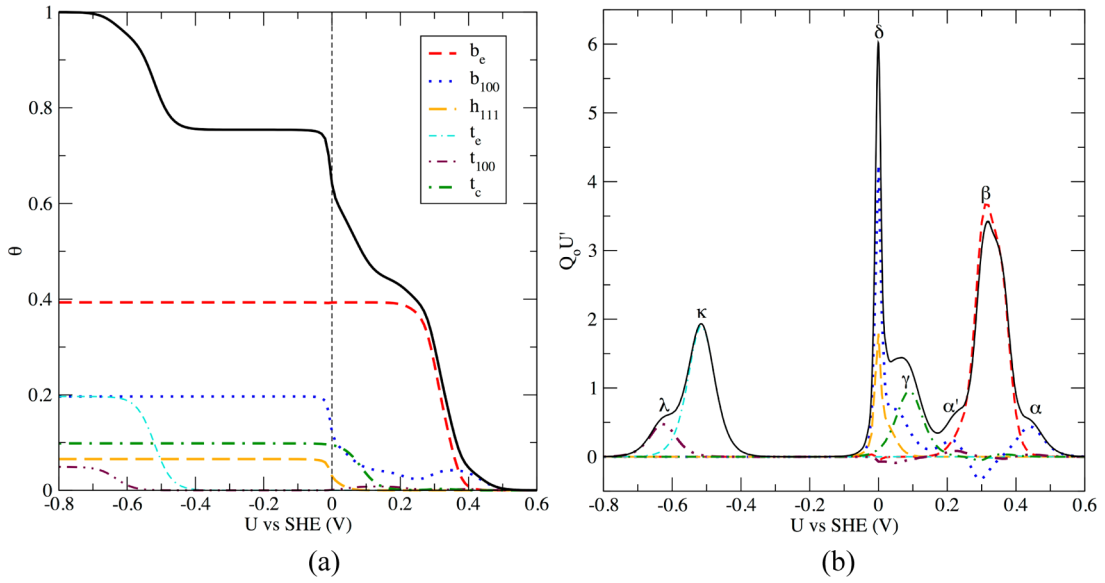

Figure 2. (a) Adsorption isotherm at standard conditions (298 K). Contributions to the total coverage (black curve) from each H* species are shown (see legend). (b) The derived cyclic voltammetry diagram. Vertical axis is in units of Q_0U'; Q_0 is total charge accumulated per Pt mass (or NP surface area) when all 122 adsorption sites are occupied by H*. U' is the voltage cycling rate. Selected peaks are labeled and are compared with those from experiments in Table 2.

versus electrochemical potential, U. The amount of adsorbed H increases as U decreases. The contributions from each of the six adsorption sites provide valuable information for the active adsorbate species during electrochemical H adsorption/desorption. The "deconvoluted" adsorption isotherm tracks the coverage of each adsorption site species, from which the fraction of potentially active sites that are available or blocked can be deduced.

At 298 K, the configuration entropic contribution is not expected to be large, and the MC simulation will sample low-energy H* configurations up to $\sim k_BT$ = 25 meV above the groundstate hull; this value of 25 meV is comparable to some of the weak H*−H* interactions but is several times smaller than the strong ones, such as those between n.n. b_{100}−b_{100}, and b_{100}−t_{100}. Hence, the observed H* configurations at each θ are not expected to deviate drastically from the groundstates. The first adsorbed H* at $\sim U$ = 0.5 V are on the b_{100}, and as U decreases to ∼U = 0.35 V, H*@b_e overtakes as the majority species and increases steadily to saturation at U = 0.15 V; θ of b_{100} meanwhile hovers at around 0.04. Adsorption at t_c and h_{111} starts at ∼0.18 and 0.06 V, respectively. A small bump in the θ of t_{100} is observed at ∼0.15 V. These observations are in line with our analysis of the groundstates, where b_e sites are expected to be fully occupied first with, at most, 1/4 of the b_{100} sites being occupied per (100) facet at the initial adsorption and then subsequent adsorption at the t_c and h_{111} sites. The adsorptions on t_e and t_{100} in the overpotential region begin at ∼−0.4 and −0.5 V, respectively.

Theoretical Cyclic Voltammetry. The adsorption isotherms are used to derive the CV curves[18,19] (see SI for derivation). The positive CV portion is shown in Figure 2b with labeled peaks together with the contributions from the individual adsorption site type. The CV profiles are often used in electrochemistry experiments as fingerprints of a specific surface structure/feature of the catalysts because the ions get adsorbed onto different sites at different voltage ranges. The location of each peak along U and their breadth indicates the adsorption species and interadsorbate repulsion, respectively, whereas their relative areas under the peak indicate the fraction of adsorption features.[30]

For experiments, the α, β, and γ peaks are associated with (100) domains, (100) step sites, and (110) step sites.[9] Our derived peak locations fit these descriptions: peak α is contributed by the b_{100} sites on the (100) facet, and β is contributed by b_e sites at the edge between the (111) and (100) facets (the so-called (100) step). Because of our cuboctahedral model, γ is contributed by t_c sites atop the corner Pt atom (at the intersection of two (111) and two (100) facets), instead of (110) step sites, had we used a truncated octahedron. Table 2 shows the peaks' locations, and they compare well with experiment, despite the smaller size of our model NP. Locations α and β are ∼0.07 and 0.05−0.1 eV more positive than those from experiment, respectively; this upshift is most likely due to the size effect, in which H adsorption on bridge sites of 1 nm particles are expected to be ∼0.1 eV stronger versus (100) surfaces.[17] Location γ differs by, at most, 0.03 eV from experiment, although we note that this peak arises from atop t_c sites instead of (110) step sites in our model. There is a

Table 2. Comparisons of CV Peaks, As Labeled in Figure 2[a]

	location of peaks (V)					
	α	β	γ	δ	shape	diam (nm)
this work	0.44	0.32	0.09	0	cubo-octa.	1.1
expt. 1[39]	n.o.	0.24	0.11	0	n.a.	2.78 ± 0.86
expt. 2[40,b]	n.o.	0.20	0.07	−0.04	cubo-octa.	4
expt. 3[37]	n.o.	0.22	0.08	n.a.	cubic	7
expt. 4[30]	0.37	0.27	0.12	n.a.	cubic	9 ± 3
expt. 5[30]	0.35	0.27	0.12	n.a.	quasi-spherical	4.0 ± 0.6

[a]The experimental CV curves are carried out in acidic environment (0.5−1 M of H_2SO_4) with voltages referenced to RHE[30,39] and NHE.[37,40] Data not available are labeled n.a., and peaks not observed are labeled n.o. [b]The results of this work may have been shifted by −0.04 eV.

DOI: 10.1021/cs501840c
ACS Catal. 2015, 5, 2376−2383

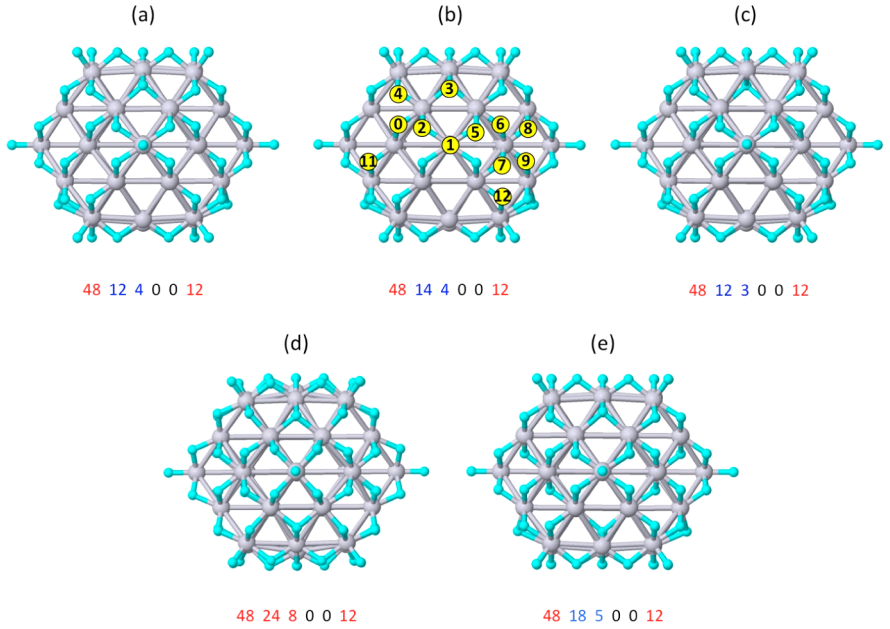

Figure 3. Five lowest-energy configurations at U = 0 ranked accordingly, (a to e), with image (a) having the lowest energy. Labeled H*'s in image (b) are considered for desorption barrier calculations (see Table 3).

peculiar contribution by b_{100} when decreasing U from 0.5 to 0.2 V. The current contribution reaches a peak at α before decreasing and reaching negative values for 0.25 V < U < 0.35 V. In this U range, the b_{100} coverage decreases while that of b_e increases rapidly. The b_{100} coverage increases (slowly) again for U < 0.25 V, resulting in a shoulder, α', at U = 0.22 V.

The relative heights of α, β, and γ compare well with the CV curves from (100)-oriented NP,[30,53] where β is the highest peak and is three times the height of α and 1.6 times that of γ. Our cuboctahedral model has a large fraction of 48 b_e sites contributing to peak β, whereas only six t_c sites (one on each (100) facet) contributes to α; hence, the β−α height ratio is around 7. We expect the β−α height ratio to be lower for larger nanoparticle models because the number of (100) facet sites will increase with respect to edge sites. We further identify the origin of a less commonly observed peak, δ, at U = 0. It arises from (i) additional adsorption on b_{100} sites, resulting in the occupation of n.n. b_{100}−b_{100} and (ii) adsorption on h_{111} sites. This peak has been observed in some experimental CVs[39,40] that reach U = 0. Peaks κ and λ, in the overpotential region, from t_e and t_{100} sites, respectively, are not accessible in experiment.

Our simulated CV compares reasonably well with experiment, despite using a small 1 nm NP. However, because of the NP size effect, the 55-atom cluster has a large proportion of atoms that are under-coordinated (42 atoms on the shell). The electronic d band (both center and width) of our 55-atom cluster is well-formed[29] (unlike few-atom clusters), but it is expected to be different from large NPs (which nears bulk-like behavior at 100+ metal atoms).[54,55] Hence, the E_{ads} of H* is expected to differ, as well. As shown previously,[17,55] for a 1 nm NP, the E_{ads} of b_{100} is ∼0.1 eV lower than that of the (100) surface, whereas that of h_{111} is ∼0.1 eV higher. Nonetheless, the E_{ads} on a semi-infinite surface is representative of the E_{ads} for large NPs, where E_{ads} converges quickly with NP size, as demonstrated by Okamoto.[55] Hence, for a large NP, we expect the location of peak α to shift negatively by ∼0.1 V, which leads to a better agreement with observations. The h_{111} contribution would be expected to shift positively by ∼0.1 V and contributes to peak γ; this may explain the higher peak seen at U = 0.1 V for spherical NPs with a higher percentage of (111) facets.[30] The E_{ads}'s for b_e sites are not expected to change much with NP size;[55] hence, peak β is expected to remain approximately at the same location.

Active H* Species During HER. At U = 0, the H coverage is representative of the Pt NP at standard operating conditions during HER.[12,19] From Figure 2a, the fractional site occupations for b_e, b_{111}, t_c, h_{111}, t_e, and t_{100} are 100%, 62%, 96%, 45%, 0%, and 2%, respectively; these values are obtained by dividing m by the number of available sites for each species. Representative low-energy H* configurations from MC simulations at U = 0 are listed in Figure 3. Using the configuration in Figure 3b, whose fractional occupation is closest to the thermodynamic one, we evaluate the activation barriers (E_a) of H_2 desorption for different pairs of H* in the Tafel reaction, eq 3. This configuration has one densely covered (100) facet with H* adsorbed on all four b_{100} sites, and the normal facets with two b_{100} sites (second n.n.) occupied. From Table 3, the low-E_a pairs are in the range of 0.69−0.75 eV and are mostly from the n.n. bridge sites on the densely covered facet; these values are comparable to that of the Pt(100) surface (0.67 eV).[50] It is surprising that the second n.n. b_{100}−b_{100} (on the normal facet) would have a low E_a of 0.75 eV. Via microkinetic modeling[12,19] (see the SI), which accounts for both the reaction barrier and the statistical occurrence (from MC simulation) of each H* pair, we estimate the exchange current (j_0) contribution from each pair. The lowest-E_a n.n. b_{100}−b_{100} pairs are the most active, contributing to 75% of total j_0. The n.n. b_e−b_{100} pairs on the dense (100) facet also contribute significantly (18% of total j_0). The overall j_0 is 1.2 × 10^{-3} A cm^{-2}, comparable to those of ideal surfaces (4.5−9.8 × 10^{-4} A cm^{-2}, depending on surface orientation[31]).

On the basis of the CV peak at U = 0, one would initially guess that b_e and h_{111} species are active species for the HER because they are weakly bound to the NP. Although the low desorption barrier of the b_e concurs with the initial guess, the

DOI: 10.1021/cs501840c
ACS Catal. 2015, 5, 2376−2383

Table 3. Activation Barriers, $E_a = E_{TS} - E_{Initial}$, for the Tafel Reaction Using Selected Pairs of H* in Figure 3b[a]

H* pairs to desorb						
type	label	E_a (eV)	E_a^{ZPE} (eV)	d_{H-H} (Å)	d_{Pt-H} (Å)	j_0 (mA cm^{-2})
t_c-b_e[b]	1, 2	0.85	0.72	n.a.	n.a.	0.01
$h_{111}-b_e$	3, 4	0.83	0.80	0.77	2.20, 2.28	0.01
$h_{111}-b_{100}$	3, 0	1.07	1.08	0.80	1.99, 2.00	0.00
b_e-b_e	2, 4	0.81	0.75	0.77	2.32, 2.31	0.03
$b_{100}-b_e$[c]	0, 2	1.01	0.95	0.78	2.23, 2.24	0.00
$b_{100}-b_e$[c]	7, 12	0.74	0.67	0.77	2.22, 2.27	0.12
$b_{100}-b_e$[c]	6, 5	0.75	0.68	0.77	2.37, 2.32	0.09
$b_{100}-b_{100}$[c]	6, 7	0.69	0.62	0.80	2.00, 1.99	0.89
$b_{100}-b_{100}$	6, 9	0.86	0.80	0.80	1.99, 1.99	0.00
$b_{100}-b_{100}$	7, 8	0.96	0.89	0.83	1.89, 1.89	0.00
$b_{100}-b_{100}$	0, 11	0.75	0.67	0.76	2.37, 2.38	0.05

[a] $E_{initial}$ and E_{TS} are the energies of the initial configuration with 78 H*'s and the transition state (TS); the final configuration has 76 H*'s and a desorbed H_2 molecule. The inter-H distance (d_{H-H}) of the desorbing pair and their distances to the NP site (d_{Pt-H}) at the TS are provided. j_0 is the estimated contribution to the exchange current based on E_a (see the SI). The zero-point corrected values for E_a are provided, as well. [b] Transition state is not available (n.a.) for this pair of H*'s; hence, $E_a = E_{final} - E_{initial}$. [c] Involving nearest neighbor bridge sites.

barrier of h_{111} with neighboring H* is high. We note that the barrier calculated here via the Tafel reaction is dependent on two neighboring H* pairs. Single-site desorption via the Heyrovsky reaction should be explored in the future where the desorption barrier of the loosely bound h_{111} species could be low.

Our computations put into perspective previous observations that the size effect adversely affects the electrocatalytic activities of very small NPs (~1−3 nm).[14,16,17] We confirm that edge sites, per se, are inactive; although b_e-b_e pairs are prevalent, their desorption barriers are high. However, b_e can participate in the HER via reaction with n.n. b_{100} species on the facet and contributes significantly to the HER, scaling with the number of b_{100} edge sites. On the other hand, the most active pairs, n.n. $b_{100}-b_{100}$ pairs, scale with the number of (100) facet sites. The 1 nm NP has a smaller ratio of active facet sites to less-active edge sites than larger NPs; hence, a decrease in activity. On the basis of such geometrical arguments[56,57] alone (see SI), one could estimate the specific (j_0) and mass (i_0) activity versus NP size. As shown in Figure 4, j_0 increases continuously with NP size, and i_0 first increases from 1 to 2.2 nm and decreases thereafter. The overall activity trend follows that of the n.n. $b_{100}-b_{100}$ species. Contributions from the edge sites (b_e) is significant for ~NP < 3 nm and diminishes with size. To reverse the adverse activity trend for NP < 2.2 nm, the E_a for b_e-b_{100} has to be lowered to become comparable with that of n.n. $b_{100}-b_{100}$. The NP size for maximum i_0 is 2.2 nm, comparable with HOR experiment (~3 nm)[14] and ORR experiment (~2.2 nm).[15] It remains to be seen how the E_a barriers on facet sites of larger NP compare with that for 1 nm NPs because a lower E_a would increase the NP size for the maximum i_0. We note that the adverse size effect predicted here is based on the caveat that the E_a of the facet pair $b_{100}-b_{100}$ is lower than that of edge pair b_e-b_e (by 0.1 eV) and the mixed pair b_e-b_{100} (by 0.05 eV), and such differences could, under certain circumstances, be sensitive to the theoretical treatment. It will be interesting to see how these values change for larger NPs to make a more complete comparison to relevant experiments.

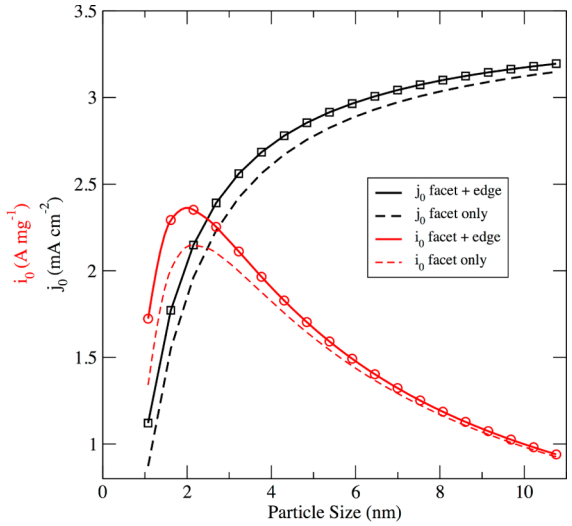

Figure 4. Activity trend versus cuboctaheral NP size. Exchange current is normalized against the NP mass and surface area for i_0 and j_0, respectively.

CONCLUSION

We predicted adsorption isotherms and derived hydrogen adsorption−desorption CV curves for Pt nanocatalysts, focusing on the 1 nm size, where the effects of size adversely affect the electrocatalytic activity. These simulations utilized DFT adsorption energies and cluster expansion thermodynamics. We elucidate the equilibrium configurations of H* adsorbed on cuboctahedral Pt nanoparticles over a wide H coverage and electrochemical potential, U. Decomposing the adsorption isotherm into site contributions, CV peaks from adsorption on b_{100} on facets, b_e at edges, and t_c at corners are identified as the experimentally observed peaks from (100) domains, (100) step sites, and the (110) step,[9] respectively. The b_e and b_{100} are occupied initially at $U > 0$ but close to $U = 0$, b_e sites are fully occupied and H starts to adsorb on t_e corner sites and the h_{111} hollow site. Atop sites t_{100} and t_c are occupied only at $U < 0$. The peak at $U = 0$ is attributed to b_e and h_{111} sites. Importantly, we are able to visualize the H* distributions at standard hydrogen electrode conditions ($U = 0$) and elucidate the active reaction species for the hydrogen evolution reaction via calculations of the activation barrier and microkinetic modeling. We show that n.n. $b_{100}-b_{100}$ H* pairs on the (100) facet are the most active species, followed by n.n. b_e-b_{100} pairs. As a result of the facet sites ($b_{100}-b_{100}$) being more active than the edge sites (b_e-b_{100}), NP displays a mass activity trend that peaks at ~2 nm, explaining why adverse effects are observed for NPs < 3 nm. Our work demonstrates the usefulness of the DFT-based cluster expansion method in modeling complex adsorbate distributions on catalyst surfaces from which active reaction species are identified via evaluation of the reaction barriers and their catalytic activity quantified via microkinetic modeling.

ASSOCIATED CONTENT

Supporting Information

The following file is available free of charge on the ACS Publications website at DOI: 10.1021/cs501840c.

DOI: 10.1021/cs501840c
ACS Catal. 2015, 5, 2376−2383

Computational details for DFT calculations. Computational details for the cluster expansion method and Monte Carlo simulations. Table and figure showing effective cluster interactions. Derivation of ZPE, vibrational free energy, and entropy terms. Derivation of theoretical cyclic voltammetry. Estimation of exchange current (PDF)

AUTHOR INFORMATION

Corresponding Author

*E-mail: tantl@ihpc.a-star.edu.sg.

Notes

The authors declare no competing financial interest.

ACKNOWLEDGMENTS

T.L.T., J.Z., and K.W.B. acknowledge internal funding from Institute of High Performance Computing (IHPC). T.L.T. and J.Z. acknowledge the use of supercomputers in A-STAR Computational Resource Centre (ACRC) for DFT computations performed in this work. The initial thesis version of TTK code, developed by T.L.T. at the University of Illinois Urbana−Champaign, was supported by the National Science Foundation (Grant DMR-012448) and the Materials Computation Center (Grant DMR-0325939). The work at Ames (TTK code for materials discovery) was supported in part by the U.S. Department of Energy (DOE), Office of Science, Basic Energy Sciences, Materials Science and Engineering Division under Contract DE-AC02-07CH11358, with additional capabilities made possible from LDRD funding for materials discovery and design. Ames Laboratory is operated for the Department of Energy by Iowa State University under Contract DE-AC02-07CH11358. Extension of TTK for catalysis (L.L.W. and D.D.J.) was supported in part by Iowa State University through a subcontract with the University of Illinois from the DOE-BES, Division of Chemical Science, Geosciences and Bioscience under Contract DEFG02-03ER15476.

REFERENCES

(1) Peng, Z.; Yang, H. *Nano Today* **2009**, *4*, 143−164.
(2) Mostafa, S.; Behafarid, F.; Croy, J. R.; Ono, L. K.; Li, L.; Yang, J. C.; Frenkel, A. I.; Cuenya, B. R. *J. Am. Chem. Soc.* **2010**, *132*, 15714−15719.
(3) Chen, J.; Lim, B.; Lee, E. P.; Xia, Y. *Nano Today* **2009**, *4*, 81−95.
(4) Cheong, S.; Watt, J. D.; Tilley, R. D. *Nanoscale* **2010**, *2*, 2045−2053.
(5) Biacchi, A. J.; Schaak, R. E. *ACS Nano* **2011**, *5*, 8089−8099.
(6) Joo, S. H.; Park, J. Y.; Renzas, J. R.; Butcher, D. R.; Huang, W.; Somorjai, G. A. *Nano Lett.* **2010**, *10*, 2709−2713.
(7) Kirubakaran, A.; Jain, S.; Nema, R. K. *Renewable Sustainable Energy Rev.* **2009**, *13*, 2430−2440.
(8) Maeda, K.; Domen, K. *J. Phys. Chem. Lett.* **2010**, *1*, 2655−2661.
(9) Koper, M. T. M. *Nanoscale* **2011**, *3*, 2054−2073.
(10) Vidal-Iglesias, F. J.; Arán-Ais, R. M.; Solla-Gullón, J.; Herrero, E.; Feliu, J. M. *ACS Catal.* **2012**, *2*, 901−910.
(11) Chen, Q.-S.; Solla-Gullón, J.; Sun, S.-G.; Feliu, J. M. *Electrochim. Acta* **2010**, *55*, 7982−7994.
(12) Skúlason, E.; Tripkovic, V.; Björketun, M. E.; Gudmundsdóttir, S.; Karlberg, G.; Rossmeisl, J.; Bligaard, T.; Jónsson, H.; Nørskov, J. K. *J. Phys. Chem. C* **2010**, *114*, 18182−18197.
(13) Nørskov, J. K.; Rossmeisl, J.; Logadottir, A.; Lindqvist, L.; Kitchin, J. R.; Bligaard, T.; Jónsson, H. *J. Phys. Chem. B* **2004**, *108*, 17886−17892.
(14) Sun, Y.; Dai, Y.; Liu, Y.; Chen, S. *Phys. Chem. Chem. Phys.* **2012**, *14*, 2278−2285.
(15) Shao, M.; Peles, A.; Shoemaker, K. *Nano Lett.* **2011**, *11*, 3714−3719.
(16) Yang, F.; Zhang, Q.; Liu, Y.; Chen, S. *J. Phys. Chem. C* **2011**, *115*, 19311−19319.
(17) Tan, T. L.; Wang, L.-L.; Johnson, D. D.; Bai, K. *Nano Lett.* **2012**, *12*, 4875−4880.
(18) Karlberg, G.; Jaramillo, T.; Skulason, E.; Rossmeisl, J.; Bligaard, T.; Nørskov, J. K. *Phys. Rev. Lett.* **2007**, *99*, 126101.
(19) Tan, T. L.; Wang, L.-L.; Johnson, D. D.; Bai, K. *J. Phys. Chem. C* **2013**, *117*, 22696−22704.
(20) Schmidt, D. J.; Chen, W.; Wolverton, C.; Schneider, W. F. *J. Chem. Theory Comput.* **2012**, *8*, 264−273.
(21) Sanchez, J. M.; Ducastelle, F.; Gratias, D. *Physica* **1984**, *128 A*, 334−350.
(22) Connolly, J. W. D.; Williams, A. R. *Phys. Rev. B* **1983**, *27*, 5169.
(23) Van de Walle, A.; Ceder, G. *J. Phase Equilib.* **2002**, *23*, 348−359.
(24) Zarkevich, N. A.; Tan, T. L.; Johnson, D. D. *Phys. Rev. B* **2007**, *75*, 104203.
(25) Lerch, D.; Wieckhorst, O.; Hammer, L.; Heinz, K.; Müller, S. *Phys. Rev. B* **2008**, *78*, 121405.
(26) Han, B. C.; Van der Ven, A.; Ceder, G.; Hwang, B.-J. *Phys. Rev. B* **2005**, *72*, 205409.
(27) Stamatakis, M.; Vlachos, D. G. *ACS Catal.* **2012**, *2*, 2648−2663.
(28) Bray, J. M.; Smith, J. L.; Schneider, W. F. *Top. Catal.* **2014**, *57*, 89−105.
(29) Wang, L.-L.; Johnson, D. D. *J. Am. Chem. Soc.* **2007**, *129*, 3658−3664.
(30) Solla-Gullón, J.; Rodríguez, P.; Herrero, E.; Aldaz, A.; Feliu, J. M. *Phys. Chem. Chem. Phys.* **2008**, *10*, 1359−1373.
(31) Marković, N. M.; Grgur, B. N.; Ross, P. N. *J. Phys. Chem. B* **1997**, *101*, 5405−5413.
(32) Marković, N. M.; Ross, P. N., Jr. *Surf. Sci. Rep.* **2002**, *45*, 117−229.
(33) Strmcnik, D.; Tripkovic, D.; van der Vliet, D.; Stamenkovic, V.; Marković, N. M. *Electrochem. Commun.* **2008**, *10*, 1602−1605.
(34) Clavilier, J.; El Achi, K.; Rodes, A. *J. Electroanal. Chem. Interfacial Electrochem.* **1989**, *272*, 253−261.
(35) Rodes, A.; El Achi, K.; Zamakhchari, M. A.; Clavilier, J. *J. Electroanal. Chem. Interfacial Electrochem.* **1990**, *284*, 245−253.
(36) Parsons, R.; Ritzoulis, G. *J. Electroanal. Chem. Interfacial Electrochem.* **1991**, *318*, 1−24.
(37) Wang, C.; Daimon, H.; Onodera, T.; Koda, T.; Sun, S. *Angew. Chem., Int. Ed.* **2008**, *47*, 3588−3591.
(38) Sánchez-Sánchez, C. M.; Solla-Gullón, J.; Vidal-Iglesias, F. J.; Aldaz, A.; Montiel, V.; Herrero, E. *J. Am. Chem. Soc.* **2010**, *132*, 5622−5624.
(39) Xing, Y. *J. Phys. Chem. B* **2004**, *108*, 19255−19259.
(40) Kinge, S.; Urgeghe, C.; De Battisti, A.; Bönnemann, H. *Appl. Organomet. Chem.* **2008**, *22*, 49−54.
(41) Kresse, G.; Furthmüller, J. *Comput. Mater. Sci.* **1996**, *6*, 15−50.
(42) Kresse, G.; Furthmüller, J. *Phys. Rev. B* **1996**, *54*, 11169−11186.
(43) Blöchl, P. E. *Phys. Rev. B* **1994**, *50*, 17953−17979.
(44) Hammer, B.; Hansen, L. B.; Nørskov, J. K. *Phys. Rev. B* **1999**, *59*, 7413−7421.
(45) Henkelman, G.; Uberuaga, B. P.; Jónsson, H. *J. Chem. Phys.* **2000**, *113*, 9901−9904.
(46) Zarkevich, N. A.; Tan, T. L.; Wang, L.-L.; Johnson, D. D. *Phys. Rev. B* **2008**, *77*, 144208.
(47) Wang, L.-L.; Tan, T. L.; Johnson, D. D. *Phys. Rev. B* **2012**, *86*, 035438.
(48) Ng, M.-F.; Tan, T. L. *Nano Lett.* **2013**, *13*, 4951−4956.
(49) Tan, T. L. *Unique Cluster Expansion for Reliable First-Principles Prediction of Alloy Thermodynamics and Phase Diagrams*; Ph.D. Thesis, University of Illinois, Urbana-Champaign, 2010.
(50) Fang, Y.-H.; Wei, G.-F.; Liu, Z.-P. *J. Phys. Chem. C* **2013**, *117*, 7669−7680.
(51) Zhang, Q.; Liu, Y.; Chen, S. *J. Electroanal. Chem.* **2013**, *688*, 158−164.

DOI: 10.1021/cs501840c
ACS Catal. 2015, 5, 2376−2383

(52) Atkins, P.; de Paula, J. *Physical Chemistry*; Oxford University Press: New York, 2010.
(53) Serrano-Ruiz, J. C.; López-Cudero, A.; Solla-Gullón, J.; Sepúlveda-Escribano, A.; Aldaz, A.; Rodríguez-Reinoso, F. *J. Catal.* **2008**, *253*, 159−166.
(54) Roduner, E. *Chem. Soc. Rev.* **2006**, *35*, 583−592.
(55) Okamoto, Y. *Chem. Phys. Lett.* **2006**, *429*, 209−213.
(56) Tritsaris, G. A.; Greeley, J.; Rossmeisl, J.; Nørskov, J. K. *Catal. Lett.* **2011**, *141*, 909−913.
(57) Tripković, V.; Cerri, I.; Bligaard, T.; Rossmeisl, J. *Catal. Lett.* **2014**, *144*, 380−388.

DOI: 10.1021/cs501840c
ACS Catal. 2015, 5, 2376−2383